

# A Compressed Sensing Strategy for Synthetic Transmit Aperture Ultrasound Imaging

Jing Liu, Qiong He, and Jianwen Luo,\* *Senior Member, IEEE*

**Abstract**—A novel beamforming technique, named compressed sensing based synthetic transmit aperture (CS-STA) is proposed to speed up the acquisition of ultrasound imaging. This technique consists of three steps. First, the ultrasound transducer transmits randomly apodized plane waves for a number of times and receives the backscattered echoes. Second, the recorded backscattered echoes are used to recover the full channel dataset of synthetic transmit aperture (STA) with a compressed sensing (CS) reconstruction algorithm. Finally, an STA image is beamformed from the recovered full STA dataset. **As CS allows recovering a signal from its few linear measurements with high probability, CS-STA is capable of recovering the STA image with fewer firings (i.e., higher frame rate) and retaining the high resolution of STA.** In addition, the contrast of the STA image can be improved at the same time owing to the higher energy of plane wave firing in CS-STA. Simulations demonstrate that CS-STA is capable of recovering the STA channel dataset with a smaller number of firings. The performance of CS-STA is evaluated in phantom experiments through comparisons with STA, multi-element STA, conventional focused mode and coherent plane wave imaging. The results demonstrate that, implemented with the same frame rate, CS-STA achieves higher or comparable resolution and contrast. Moreover, comparisons are conducted on the biceps brachii muscle and thyroid of a human subject, and the results demonstrate the feasibility and competitiveness of CS-STA in the *in vivo* conditions.

**Index Terms**—Compressed sensing, contrast, frame rate, resolution, synthetic transmit aperture, ultrasound imaging.

## I. INTRODUCTION

COMPRESSED sensing (CS) or compressive sampling states that if a signal  $\mathbf{x} \in \mathbf{R}^n$  is sparse or compressible in one domain, it can be faithfully reconstructed from its fewer (e.g.,  $m, m < n$ ) linear combinations  $\mathbf{y} \in \mathbf{R}^m$  expressed as the multiplication of a measurement matrix  $\Phi \in \mathbf{R}^{m \times n}$  and  $\mathbf{x}$  [1]. The measurement matrix  $\Phi$  is usually random to some extent to guarantee the reconstruction performance [2]. Because of

this attractive advantage, CS has been successfully applied to diverse fields, including the field of medical imaging [3]–[5].

One of the most successful CS applications in medical imaging is rapid magnetic resonance (MR) imaging [3]. In this application, the measurement matrix  $\Phi$  is a random partial Fourier matrix and this CS sampling strategy is suitable for MR imaging. Although ultrasound imaging is much faster than MR imaging and meets the real-time demands in most applications, some particular applications, such as cardiac motion and deformation imaging [6], [7], blood flow imaging [8], and three-dimensional (3D) imaging [9], need higher frame rate. Researchers have explored methods to improve the frame rate from different points of view [10]–[12]. **However, there is a trade-off between the frame rate and image quality among these methods.** Since CS has shown its great capability in rapid MR imaging, whether it can achieve simultaneously high frame rate and high image quality or achieve a better trade-off between the frame rate and image quality in ultrasound imaging remains to be a question. Recently, several studies have been carried out to answer this question.

To achieve higher frame rate in ultrasound imaging with CS, it is crucial to develop a CS sampling strategy to adapt the way of data acquisition in ultrasound systems. As an ultrasound image is typically acquired line by line, a CS way to reduce the acquisition time is down-sampling the image lines randomly [13]. In this method, each row of the measurement matrix  $\Phi$  has an entry one at a random position and zero elsewhere. The measurement matrix is different from that in the MR applications because ultrasound image is acquired in the spatial domain, rather than the spatial frequency domain (i.e., the  $k$ -space). **This method has achieved promising results in 3D ultrasound imaging, especially when dictionary learning is adopted to determine the sparse basis** [14].

In ultrasound imaging, the received signal is actually the collections of the echoes backscattered by all the scatterers in the image area. In other words, the received signal is the linear combinations of reflectivities (or other imaging parameters) of all the scatterers. As a result, the reflectivities can be reconstructed using the CS method under the assumption that the reflectivities can be sparsely represented. As the backscattered echoes can be acquired with one plane wave firing, ultrafast ultrasound imaging is achieved [15]. The key to this method is to determine the linear combination coefficients of reflectivities, i.e., the measurement matrix  $\Phi$ . For this problem, researchers have proposed different methods to calculate the measurement matrix  $\Phi$  based on acoustic wave equation or

Manuscript received August 3, 2016; revised September 27, 2016 and December 11, 2016; accepted December 20, 2016. Date of publication December 23, 2016; date of current version April 1, 2017. This study was supported in part by the National Natural Science Foundation of China (61322101, 61271131, and 81471665 and 81561168023) and the National Key R&D Program of China (2016YFC0102201 and 2016YFC0104705). *Asterisk indicates corresponding author.*

J. Liu and Q. He are with the Department of Biomedical Engineering, School of Medicine, Tsinghua University, Beijing 100084, China.

\*J. Luo is with the Department of Biomedical Engineering, School of Medicine, Tsinghua University, Beijing 100084, China (e-mail: luo\_jianwen@tsinghua.edu.cn).

Digital Object Identifier 10.1109/TMI.2016.2644654

spatial impulse response of ultrasound in the time or frequency domain [15]–[18]. It should be noted that there are some other CS applications in ultrasound imaging [19]–[25] besides the above applications for improving the frame rate.

For all the CS applications in ultrasound imaging, there is a premise that the ultrasound signal should be sparsely represented in a sparse basis. The sparse basis may vary for different kinds of ultrasound signals. Liebgott *et al* have studied the reconstruction performance of pre-beamformed ultrasound radio-frequency (RF) signal in different sparse bases [21]. The results demonstrate that choosing the wave atoms as the sparse basis, the reconstruction has the minimum error. For ultrafast ultrasound imaging with CS, Schiffner *et al* have studied the reconstruction performance of spatial fluctuation in the Fourier and wavelet bases [26]. The results show that the spatial fluctuation can be better reconstructed with the Daubechies-20 wavelet than with the Fourier basis. Because different kinds of signals have their optimum sparse basis, the specific signal may not be most sparsely represented with the existing fixed basis. To solve this issue, with a learning process, the over-complete dictionary has been employed to represent the specific signal as sparsely as possible [14].

Once the measurement matrix and sparse basis are determined, the reconstruction can be performed by searching the sparsest solution with suitable optimization algorithm. In most CS applications in ultrasound imaging, the sparsest solution is achieved by minimizing the  $l_p$  ( $p = 1$ ) norm. With the knowledge that the tissue reflectivity function can be well regularized by a generalized Gaussian distribution, minimizing  $l_p$  ( $1 \leq p \leq 2$ ) norm is adopted in the CS application in ultrasound deconvolution as well [25].

In this paper, a CS strategy, named compressed sensing based synthetic transmit aperture (CS-STA) is proposed to achieve simultaneously high frame rate and high image quality in ultrasound imaging. Synthetic transmit aperture (STA) is an established method in which each element is activated sequentially to transmit an ultrasound wave and all the elements receive the backscattered echoes [27]. CS-STA is realized by transmitting several plane waves with different random transmit apodizations. The backscattered echo of each plane wave (PW) firing is a linear combination of the full STA channel dataset and the linear combination coefficients are the transmit apodizations applied in the PW firings. As a result, the full STA channel dataset can be recovered from fewer randomly apodized PW firings with the CS reconstruction algorithm. The random apodizations applied in the PW firings compose the measurement matrix  $\Phi$  of the CS theory. The concept of CS-STA has been introduced briefly in our preliminary work [28], in which we studied the recovery performance of CS-STA without noise for the simulated point-target phantom and compared CS-STA with the traditional focused mode and STA methods qualitatively through phantom experiments. In this paper, we provide more theoretical foundations for understanding and implementing CS-STA and perform more comprehensive validations in simulations with and without noise for the point-target and cyst phantoms. Besides, comparisons with more methods were conducted through quantitative phantom experiments and qualitative *in vivo* experiments.

Furthermore, the performance of CS-STA is fully discussed in this work.

This paper is organized as follows. In Section II, the acoustic theory of CS-STA is derived. The feasibility of CS-STA is studied with simulation experiments in Section III. In Sections IV and V, the performance of CS-STA is evaluated through the comparisons with other methods in phantom experiments and preliminary *in vivo* experiments, respectively. Sections VI and VII discuss and conclude this work, respectively.

## II. COMPRESSED SENSING BASED SYNTHETIC TRANSMIT APERTURE

In this section, the mathematical relationship between the channel datasets of STA and PW is derived. Based on this relationship and the CS theory, the CS-STA method is described afterwards. For STA, an individual element is active in each firing and all the elements receive the backscattered echoes, and this process is repeated by choosing each element as the transmitter sequentially [27]. For a PW firing, all the elements are active in each transmission and reception [29].

### A. Mathematical Relationship Between STA and PW Firing

For simplicity, consider an arbitrary point  $P$  with a unitary scattering intensity in the imaging space. There is an  $n$ -element transducer and  $\vec{r}_i$  is the vector from the  $i^{\text{th}}$  element ( $i = 1, 2, \dots, n$ ) to point  $P$ . Because the first-order Born approximation is employed, the temporal transmit impulse response  $h_{tx}(i, t)$  for the  $i^{\text{th}}$  element to the point  $P$  can be expressed as [30]:

$$h_{tx}(i, t) = a_{tx}(i) \frac{\delta\left(t - \frac{|\vec{r}_i|}{c}\right)}{|\vec{r}_i|} \quad (1)$$

where  $a_{tx}(i)$  is the transmit apodization applied to the  $i^{\text{th}}$  transmit element,  $\delta(t)$  is the Dirac function. Eq. (1) can be seen as the temporal transmit impulse response of each STA firing, in which only one element is active.

Furthermore, it is assumed that the ultrasound pulse-echo transfer function is linear, i.e., the response of the ultrasound array is the summation of those of all the elements. When all the elements are active in each transmission, the temporal transmit impulse response  $h_{tx}(t)$  can be expressed as [30]:

$$h_{tx}(t) = \sum_{i=1}^n h_{tx,i}(t) = \sum_{i=1}^n a_{tx}(i) \frac{\delta\left(t - \frac{|\vec{r}_i|}{c}\right)}{|\vec{r}_i|} \quad (2)$$

Eq. (2) can be seen as the temporal transmit impulse response of a PW firing.

The backscattered echoes (i.e., channel data)  $p(k, t)$  received by the  $k^{\text{th}}$  receive element can be expressed as [31]:

$$p(k, t) = \frac{1}{c_0^2} \frac{\partial^2 v_{pe}(t)}{\partial t^2} *_t h_{tx}(t) *_t h_{rx}(k, t) \quad (3)$$

where  $*$  denotes the convolution operation in the time domain,  $v_{pe}(t)$  is the pulse-echo electromechanical impulse response

including the excitation function, and  $h_{tx}(t)$  and  $h_{rx}(k, t)$  are the temporal transmit and receive impulse responses, respectively. As only the echoes received by the  $k^{\text{th}}$  receive element is considered,  $h_{rx}(k, t)$  is calculated as Eq. (1) because of the reciprocity between transmission and reception.  $h_{tx}(t)$  is different for different imaging modes. For a PW firing,  $h_{tx}(t)$  is calculated as Eq. (2) and therefore, substituting Eqs. (1) and (2) to Eq. (3), the echoes received by the  $k^{\text{th}}$  element  $p_{PW}(k, t)$  is given by:

$$p_{PW}(k, t) = \sum_{i=1}^n a_{tx}(i) \frac{a_{rx}(k)}{|\vec{r}_i| |\vec{r}_k|} e \left( t - \frac{|\vec{r}_i|}{c} - \frac{|\vec{r}_k|}{c} \right) \quad (4)$$

where  $e(t)$  represents that term of  $\frac{1}{c^2} \frac{\partial^2 v_{pe}(t)}{\partial t^2}$  in Eq. (3). For the  $i^{\text{th}}$  STA firing,  $h_{tx}(t)$  is calculated as Eq. (1) and  $a_{tx}(i) = 1$ . As a result, the echoes  $p_{STA}(i, k, t)$  received by the  $k^{\text{th}}$  element for the  $i^{\text{th}}$  STA firing is given by:

$$p_{STA}(i, k, t) = \frac{a_{rx}(k)}{|\vec{r}_i| |\vec{r}_k|} e \left( t - \frac{|\vec{r}_i|}{c} - \frac{|\vec{r}_k|}{c} \right) \quad (5)$$

Comparing Eqs. (4) and (5), it can be found that:

$$p_{PW}(k, t) = \sum_{i=1}^n a_{tx}(i) p_{STA}(i, k, t) \quad (6)$$

That is to say, the echoes received by the  $k^{\text{th}}$  element for a PW firing is a linear combination of the echoes received by the same element for all the STA firings, and the linear combination coefficients are the transmit apodization applied in the PW firing. This relationship holds for an arbitrary point  $P$  with a unitary scattering intensity. As a result, according to the superposition principle, it can be expanded to the general case where the imaging space consists of numbers of points with scattering intensity  $f(p)$ .

## B. Compressed Sensing Based Synthetic Transmit Aperture

Fig. 1 presents the STA and CS-STA sequences. In each CS-STA firing, a PW with a random transmit apodization is transmitted. The relationship given by Eq. (6) exists in each CS-STA firing and is illustrated in Fig. 1. It can be written as below when  $t$  is discretized:

$$p_{CS-STA}(j, k, d) = \sum_{i=1}^n a_{tx}(j, i) p_{STA}(i, k, d) \quad (7)$$

where  $j$ ,  $k$ , and  $d$  are the CS-STA firing, receive element, and sample indexes, respectively, and  $a_{tx}(j, i)$  is the transmit apodization applied on the  $i^{\text{th}}$  element in the  $j^{\text{th}}$  CS-STA firing.

For receive element  $k$  and sample index  $d$ , the slow time signal of CS-STA is given by:

$$\begin{aligned} \mathbf{y} &= (y_1, \dots, y_j, \dots, y_m) \\ &= (p_{CS-STA}(1, k, d), \dots, p_{CS-STA}(j, k, d), \dots, \\ &\quad p_{CS-STA}(m, k, d)) \end{aligned} \quad (8)$$

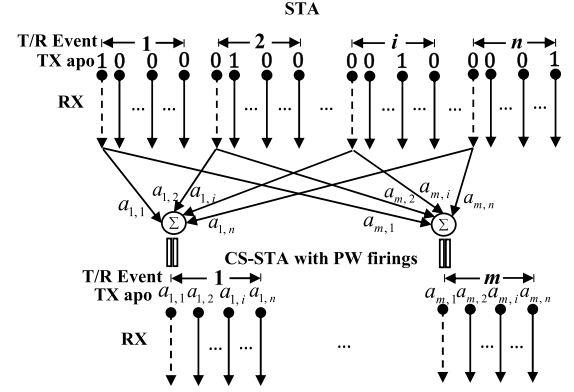


Fig. 1. The sequences of STA and CS-STA. For an  $n$ -element array, STA and CS-STA consist of  $n$  and  $m$  ( $m < n$ ) transmit/receive events, respectively. The transmit apodizations (0 or 1 for STA firing,  $a$  for PW firing) are denoted by TX apo. The receive event is denoted by RX (with all the element receiving for both STA and CS-STA) and the received channel data are presented as the upright arrows. The dashed arrows are used to describe that the channel data received by the first channel of a PW firing is the linear combination of those received by the same channel of all the STA firings. The combination coefficients are the corresponding transmit apodization in the PW firing.

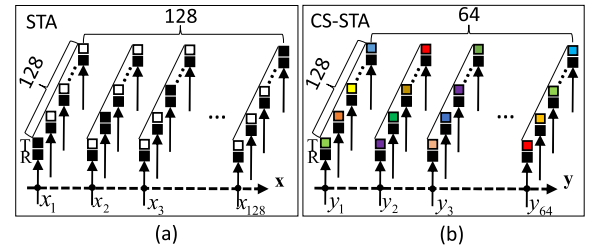


Fig. 2. An example of the slow time signal of STA  $\mathbf{x}$  (a) and CS-STA  $\mathbf{y}$  (b) when  $n = 128$  and  $m = 64$ . The colored rectangular boxes indicate the apodization amplitudes; white and black correspond to 0 and 1, respectively, and the other colors correspond to random numbers between 0 and 1.  $\mathbf{x}$  or  $\mathbf{y}$  consists of the samples for the same sample index and receive element from all firings sequentially.

while the slow time signal of STA is given by:

$$\begin{aligned} \mathbf{x} &= (x_1, \dots, x_i, \dots, x_n) \\ &= (p_{STA}(1, k, d), \dots, p_{STA}(i, k, d), \dots, p_{STA}(n, k, d)) \end{aligned} \quad (9)$$

Fig. 2 illustrates an example of  $\mathbf{x}$  and  $\mathbf{y}$  when  $m = 64$  and  $n = 128$ . By substituting  $\mathbf{x}$  and  $\mathbf{y}$ , Eq. (7) is rewritten as:

$$\mathbf{y} = \Phi \mathbf{x} \quad (10)$$

where the  $j^{\text{th}}$  row of  $\Phi$  comprises the transmit apodization applied in the  $j^{\text{th}}$  CS-STA firing  $a_{tx}(j, i)$ . It is found that Eq. (10) is the compressive sampling process in the CS theory if  $m < n$  and  $\Phi$  is the measurement matrix [1], [2].

Assuming that  $\mathbf{x}$  (i.e., the slow time signal of STA) can be sparsely represented in a sparse basis  $\Psi$ , as,

$$\mathbf{x} = \Psi \mathbf{v} \quad (11)$$

where most entries of  $\mathbf{v} \in \mathbf{R}^n$  (i.e., the sparse representation of  $\mathbf{x}$ ) are zero. Substituting Eq. (11) into (10), we can obtain,

$$\mathbf{y} = \Phi \Psi \mathbf{v} = \Theta \mathbf{v} \quad (12)$$



where  $\Theta = \Phi\Psi$ . When sufficient entries of  $\mathbf{v}$  are zero, it is possible to reconstruct it by solving the following convex optimization problem [1], [2],

$$\hat{\mathbf{v}} = \underset{\mathbf{v} \in \mathbf{R}^n}{\mathbf{arg\,min}} \|\mathbf{v}\|_1 \quad \text{subject to} \quad \|\mathbf{y} - \Theta\mathbf{v}\|_2 \leq \varepsilon \quad (13)$$

where  $\varepsilon$  is the tolerated error,  $\|\cdot\|_1$  and  $\|\cdot\|_2$  are the  $l_1$  and  $l_2$  norm operations, respectively. Substituting  $\mathbf{v}$  into Eq. (11), the slow time signal of STA  $\mathbf{x}$  can be recovered. In CS-STA application,  $\mathbf{v}$  is not sparse but compressible (i.e.,  $\mathbf{v}$  decays exponentially and most its entries are very small). Therefore, the solution found by Eq. (13) gives the approximation of  $\mathbf{v}$  by keeping its largest entries. There is a constraint criterion that the measurement matrix  $\Phi$  and the sparse basis  $\Psi$  are incoherent [32]. This property guarantees that the measurement signal  $\mathbf{y}$  retains the information of the original signal as much as possible, and therefore can be used to recover  $\mathbf{x}$  based on the CS reconstruction algorithm. This condition is often satisfied when  $\Phi$  obeys a random distribution [2], that is why the transmit apodization applied in each PW firing of CS-STA is random. It should be noted that, strictly speaking, it is not plane wave any more if a random apodization is applied. However, for the sake of brevity, the term of “randomly apodized plane wave” is used in this paper.

The workflow of CS-STA can be summarized as below:

- 1) Acquire the channel dataset of  $m$  CS-STA firings (randomly apodized PW firings).
- 2) Retrieve the slow time signal of CS-STA  $\mathbf{y}$  for receive element  $k$  and sample index  $d$  according to Eq. (8) or Fig. 2.
- 3) Reconstruct the slow time signal of STA  $\mathbf{x}$  defined by Eq. (9) from  $\mathbf{y}$  for the same receive element  $k$  and sample index  $d$  using the CS reconstruction algorithm.
- 4) Recover the full STA channel dataset by repeating steps 2) and 3) for all receive elements and sample indexes ( $k = 1, 2, \dots, n$ , and  $d = 1, 2, \dots, 2 \times \text{depth} \times f_s / c$ , where  $c$  is the speed of ultrasound and  $f_s$  is the sampling frequency).
- 5) Form the ultrasound image by performing a standard STA beamforming on the recovered full STA dataset from step 4).

Specifically, in step 1) in this work, the transmit apodizations or measurement matrix  $\Phi$  obey a continuous uniform distribution with the amplitudes being randomly distributed in the interval of  $[0, 1]$  and the mean value being 0.5, i.e.,  $\Phi \sim U(0, 1)$ . It can be designed in advance and then written to the hardware such as random-access memory. When the transducer transmits an apodized plane wave, the corresponding apodization can be read from the hardware. In step 3), the SPGL1 solver [33]–[35] is used to recover the slow time signal of STA  $\mathbf{x}$  in this paper. The *sym8* wavelet [36] is chosen as the sparse basis  $\Psi$  and the tolerated error  $\varepsilon$  is empirically set as  $1 \times 10^{-3}$  in all the simulations, phantom and *in vivo* experiments in this paper. Considering that its amplitude varies with different acquisition systems or imaging objects, the measurement signal  $\mathbf{y}$  is normalized to its  $l_1$  norm first before being input to the solver so that a fixed tolerated error  $\varepsilon$  can be used. Then, the output is multiplied by the  $l_1$  norm of  $\mathbf{y}$

to maintain the amplitude of the sparse representation  $\mathbf{v}$  of the slow time signal  $\mathbf{x}$  of the STA data. In step 5), the receive f-number is 1.5 and a rectangular window is used as the receive apodization function in this paper.

### III. SIMULATIONS

In this section, the recovery performance of the CS-STA method at different frame rates was investigated with computer simulations in the Field II environment [37], and the B-mode images of CS-STA were compared with those of STA. Different frame rates were obtained by changing the number of CS-STA firings.

#### A. Simulation Setup

A 128-element linear array transducer with a pitch of 0.3 mm was simulated. The center frequency and sampling frequency were 7.5 MHz and 100 MHz, respectively. Two types of phantoms with no acoustic attenuation were simulated. In the first phantom, six point targets were placed sequentially 10 mm apart along the center axis. The second phantom consisted of three hyperechoic regions and three hypoechoic cyst regions. There were  $1 \times 10^5$  scatterers in a  $60 \times 40 \times 15 \text{ mm}^3$  space (axial  $\times$  lateral  $\times$  elevational). This scatterer density was the same as the cyst phantom example of Field II.

For each phantom, the full STA dataset and the backscattered echoes of CS-STA were simulated. To study the effects of the number of apodized plane wave firings on the CS recovery performance, the full dataset of these two phantoms were recovered from different numbers (i.e., 32, 64, 96 and 128) of plane wave firings. Throughout this paper, CS32-STA, CS64-STA and CS96-STA mean the CS-STA method with 32, 64 and 96 plane wave firings, respectively. For the sake of convenience, CS128-STA is used to represent the use of 128 apodized plane wave firings combined with the same CS reconstruction algorithm. However, this critical case is not actually a CS application because it is not underdetermined. In addition, Gaussian noise with different signal-to-noise ratios (SNRs), i.e., 10, 20, 30, 40, and 50 dB, was added to the backscatter echoes of CS32-STA, CS64-STA, and CS96-STA to study the denoising performance of CS-STA.

#### B. Simulation Results

For the simulated point-target phantom, the B-mode images of CS-STA with different numbers of firings without noise are compared with the image of STA in Fig. 3. All the B-mode images have a dynamic range of 50 dB in this paper. The images of CS64-STA, CS96-STA and CS128-STA are found to be very close to the STA result, but the image of CS32-STA is polluted with visible artifacts. These artifacts are reduced by increasing the number of plane wave firings (see the results of CS64-STA, CS96-STA and CS128-STA). Fig. 4 shows the B-mode images of STA and CS-STA for the simulated cyst phantom. The image of CS32-STA has some visible artifacts especially in the hypoechoic (cyst) region. Again, these artifacts are reduced in the B-mode images of CS64-STA, CS96-STA, and CS128-STA. It should be noted

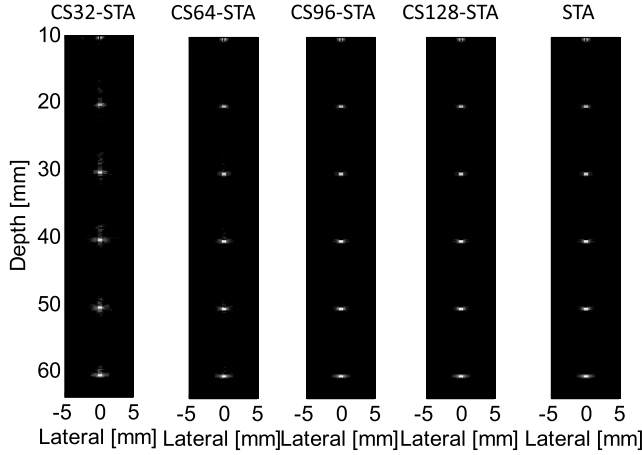


Fig. 3. B-mode images of STA and CS-STA with different numbers of firings for the simulated point-target phantom with a 50 dB dynamic range.

that there is visible bright noise on the right side of the cyst at the depth of 25 mm in Fig. 4. It is the consequence of the grating-lobe noise, rather than being an effect of the proposed CS-STA method, because the pitch (0.3 mm) is greater than the ultrasound wavelength (0.2 mm). This noise can be seen in the STA image as well.

The difference between the B-mode image of CS-STA and STA results from the CS recovery error. The recovered echoes of the point and cyst phantoms from CS64-STA are compared with those from STA in Figs. 5(a) and 5(b). In each figure, the echoes are both normalized to the maximum value of the corresponding STA echoes. As can be seen, most echoes are recovered accurately. However, the recovered echoes show slight reductions in amplitude and small differences in phase, which are more evident in the cyst phantom [Fig. 5(b)]. To quantify the recovery error, the normalized root-mean-square errors (NRMSEs) between the full channel STA dataset and its recovered version from CS-STA (NRMSE<sub>ch</sub>) are calculated as below:

$$\text{NRMSE}_{\text{ch}} = \frac{\sqrt{\frac{1}{N_e N_r N_s} \sum_{i=1}^{N_e} \sum_{j=1}^{N_r} \sum_{k=1}^{N_s} (rf'_{\text{ch}}(e_i, r_j, s_k) - rf_{\text{ch}}(e_i, r_j, s_k))^2}}{\max_{i,j,k} |rf_{\text{ch}}(e_i, r_j, s_k)|} \quad (14)$$

where  $rf_{\text{ch}}(e_i, r_j, s_k)$  and  $rf'_{\text{ch}}(e_i, r_j, s_k)$  denote the backscattered data of STA and the recovered data from CS-STA, respectively,  $e_i, r_j$  and  $s_k$  are the active transmit element, receive element and sample indexes, respectively, and  $N_e, N_r$  and  $N_s$  are the numbers of transmit elements, receive elements and samples, respectively. In this study,  $N_e$  and  $N_r$  are both 128, and  $N_s$  is 6,973 and 9,241 for the point-target and cyst phantoms, respectively.

To quantify the recovery error after beamforming, the NRMSEs between the beamformed RF data of STA and

CS-STA (NRMSE<sub>bf</sub>) are also calculated as,

$$\text{NRMSE}_{\text{bf}} = \frac{\sqrt{\frac{1}{N_l N_s} \sum_{i=1}^{N_l} \sum_{k=1}^{N_s} (rf'_{\text{bf}}(l_i, s_k) - rf_{\text{bf}}(l_i, s_k))^2}}{\max_{i,k} |rf_{\text{bf}}(l_i, s_k)|} \quad (15)$$

where  $rf_{\text{bf}}(l_i, s_k)$  and  $rf'_{\text{bf}}(l_i, s_k)$  denote the beamformed RF data from STA and CS-STA, respectively,  $l_i$  and  $s_k$  are the RF line and sample indexes, respectively, and  $N_l$  and  $N_s$  are the numbers of RF lines and samples, respectively. In this study,  $N_l = 128$ . The NRMSEs of the point-target and cyst phantoms are shown in Fig. 6. It can be seen that NRMSE decreases with the number of CS-STA firings. It means that the recovery is more accurate when more firings are used. The NRMSE<sub>ch</sub> of CS32-STA for the point-target phantom is 0.98%, higher than those of CS64-STA (0.42%), CS96-STA (0.12%), and CS128-STA ( $9.19 \times 10^{-3}\%$ ). After beamforming, the recovery errors are reduced; and the NRMSE<sub>bf</sub> of CS32-STA and CS64-STA are 0.41% and 0.12%, respectively. This trend can be observed for the cyst phantom in Fig. 6(b) as well. Comparing the point-target with cyst phantom, we find that the NRMSE of the point-target phantom is smaller than that of the cyst phantom. However, after beamforming, the NRMSEs for both phantoms are less than 1% when the number of firing is larger than 64.

The NRMSE<sub>bf</sub> of CS-STA with different SNR levels are plotted in Fig. 7. As shown, the NRMSE decreases with the increase of the SNR. The NRMSEs without noise are also plotted. It can be seen that for the point-target phantom, when the SNR increases to 20 dB, the NRMSE<sub>bf</sub> is close to that of CS-STA without noise. When the SNR increases further, e.g., larger than 30 dB, CS-STA achieves the same NRMSE as the noise-free condition. This phenomenon exists for CS-STA with 32, 64, and 96 firings. Similar results can also be observed in the results of the cyst phantom. Compared with the result of the point-target phantom, the NRMSEs for the cyst phantom converge to the noise-free conditions faster. These results demonstrate that CS-STA is capable of remaining its performance in the noisy conditions, and it is more robust in the cyst phantom than in the point-target phantom.

#### IV. PHANTOM EXPERIMENTS

The simulations have demonstrated that with a smaller number of firings, CS-STA is capable of recovering the STA channel dataset. These results are expected, because the same assumptions are adopted in the Field II simulator and the establishment of CS-STA. In this section, CS-STA is validated in phantom experiments with a real ultrasound acquisition system.

##### A. Experimental Setup

The proposed CS-STA method was compared with the conventional focused mode, STA, multi-element synthetic transmit aperture (ME-STA) [12], [38], and coherent plane wave (CPW) imaging [11] on a multi-purpose tissue-mimicking phantom (model 040GSE, CIRS, Norfolk,

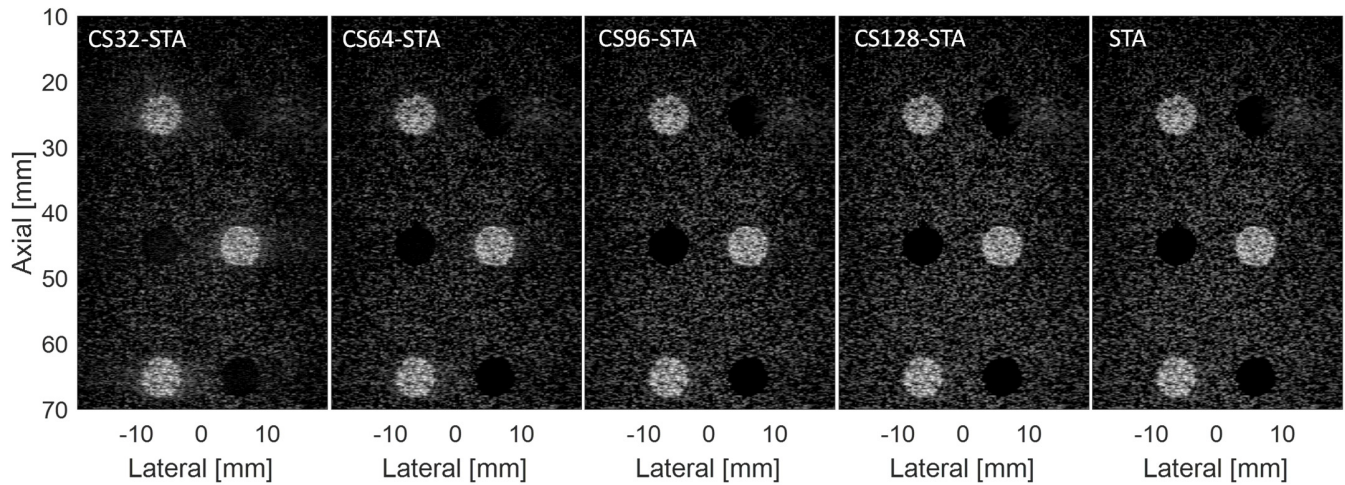


Fig. 4. B-mode images of STA and CS-STA with different numbers of firings for the simulated cyst phantom with a 50 dB dynamic range.

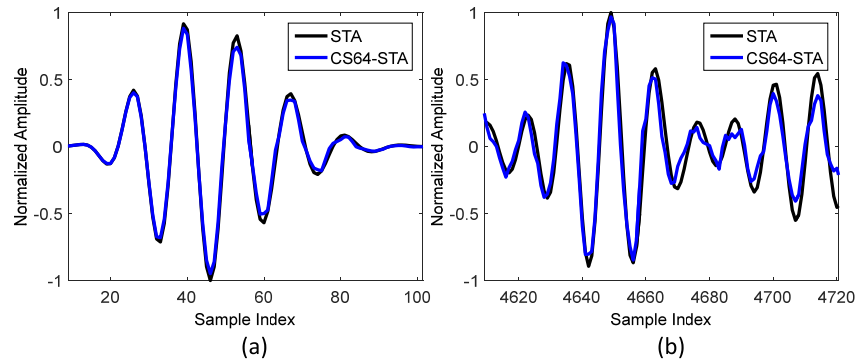


Fig. 5. (a) and (b) are zoomed-in comparisons of the normalized backscattered echoes of STA and the recovered backscattered echoes from CS64-STA for the simulated point-target and cyst phantoms, respectively. The black line represents the backscattered echoes of STA and the blue line represents the recovered backscattered echoes from CS64-STA. Both of them are normalized to the maximum value of the STA data.

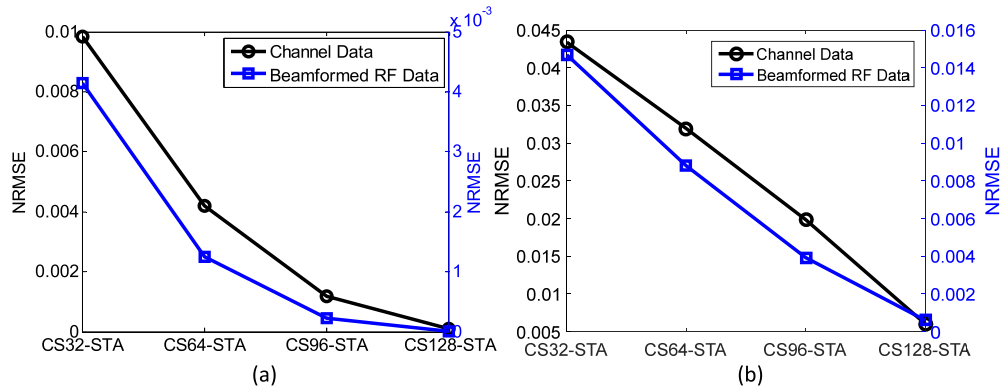


Fig. 6. (a) and (b) are the normalized root-mean-square error (NRMSE) between STA and CS-STA for the simulated point-target and cyst phantoms, respectively. The black curve denotes the NRMSEs of the channel dataset between STA and CS-STA with different numbers of firings. The blue curve denotes the NRMSEs of the beamformed RF data between STA and CS-STA with different numbers of firings.

VA, USA). Two regions (i.e., a wire region and a cyst region) with an acoustic attenuation of 0.5 dB/cm/MHz were illuminated for the evaluation of the spatial resolution and contrast resolution. The backscattered echoes (channel data) of the above five modes were sampled at 30 MHz with a Verasonics V1 system (Verasonics Inc., Redmond, WA,

USA) equipped with a 128-element linear-array transducer (L10-5, Shenzhen JiaRui Co., Shenzhen, China). The pitch and center frequency of the transducer were 0.3 mm and 7.5 MHz, respectively.

STA and the focused mode were implemented with the lowest frame rate in this study, and the number of firings



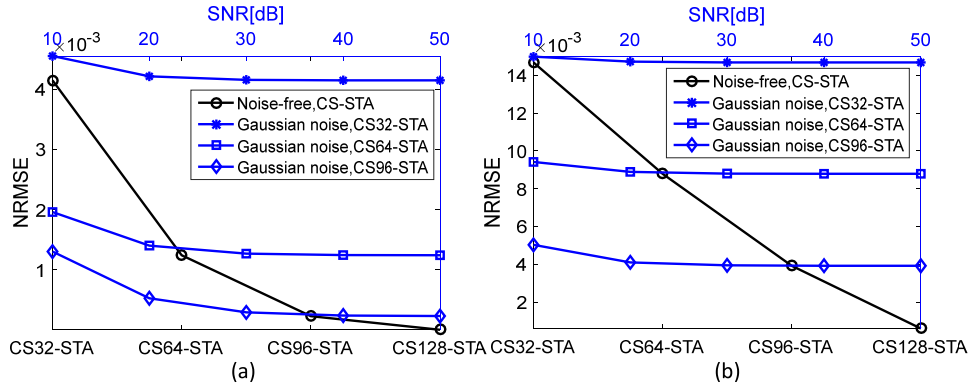


Fig. 7. (a) and (b) are the normalized root-mean-square error (NRMSE) between the beamformed RF data of STA and CS-StA for the simulated point-target and cyst phantoms with different signal-to-noise (SNR) levels, respectively. The black curve denotes the NRMSEs of the beamformed RF data of STA and CS-StA with different firings without noise. The blue curves denoted the NRMSEs of the beamformed RF data between STA and CS-StA with different SNR levels.

was 128. The focal distance and transmit f-number of the focused mode were 20 mm and 2, respectively. CPW and CS-StA were implemented with twice and four times higher frame rates (64 and 32 firings), referred to as CPW64, CPW32, CS64-StA, and CS32-StA, respectively. To keep the same frame rates as CS64-StA and CS32-StA, ME-StA was realized by activating a sub-aperture with 4 elements each time and then shifting to the next 4 elements with or without a 2-element overlap, resulting in 63 (ME63-StA) or 32 (ME32-StA) firings, respectively. The 4-elements sub-aperture was activated to transmit a diverging wave and the defocused source was located 2.2 mm behind the sub-aperture. The steering angles of CPW imaging were generated by equally dividing  $-10^\circ$  to  $10^\circ$  (64 firings, CPW64) and  $-5^\circ$  to  $5^\circ$  (32 firings, CPW32), respectively. To increase the CNR of STA and ME-StA, 50 V was applied to the elements, while 12 V was applied in the other modes. Only default filters of the V1 system were employed, without any other filter operations in the processing step. The backscattered echoes of CS-StA were firstly normalized before being input to the SPGL<sub>1</sub> solver. With the acquired channel data, the delay-and-sum beamforming was employed to produce the B-mode images. The receive f-number was 1.5 and a rectangular window was used as the receive apodization function for all the methods.

## B. Experimental Results

Figs. 8 and 9 present the B-mode images of different regions of the phantom. The STA images are affected by noise, especially at the depths over 30 mm, while the effect of noise is smaller in the ME-StA images. The focused mode performs better in the focal region than in other regions. The images of CPW are a little dark, but they appear to have good resolution for the wire targets [Figs. 8(d) and 8(g)] and good visibility of the cyst at shallow depths [Figs. 9(d) and 9(g)]. The images of CS-StA are bright and the wire targets are clear [Figs. 8(e) and 8(h)], but the cyst is a little difficult to see for CS32-StA [Fig. 9(h)].

The full width at half-maximum (FWHM) of the wire targets and contrast-to-noise ratio (CNR) are used to evaluate the

spatial resolution and contrast resolution of different methods. The CNR (in dB) for a B-mode image is calculated as follows:

$$\text{CNR} = 20 \cdot \log_{10} \left( \frac{|\mu_c - \mu_b|}{\sqrt{\sigma_c^2 + \sigma_b^2}} \right) \quad (16)$$

where  $\mu_c$  and  $\sigma_c$  are the mean and standard deviation of the intensities in the target region, and  $\mu_b$  and  $\sigma_b$  are the mean and standard deviation of the intensities in the background region. The hyperechoic and cyst regions and their corresponding background regions used in the CNR calculation are marked with the yellow and white rectangular boxes in Figs. 8(d) and 9(d), respectively. The FWHMs near the depths of 20 and 50 mm [indicated by the yellow arrows marked with A and B in Fig. 8(d)] and the CNRs of the hyperechoic and cyst regions are shown in Table I.

For wire target A, the FWHMs are all around 0.45 mm, except that of CPW32 (0.50 mm). For wire target B, the FWHMs of the focused mode and STA are 0.58 and 0.43 mm, respectively. They are of the lowest frame rate ( $\sim 100$  Hz) in this study. The FWHMs of ME63-StA, CPW64, and CS64-StA are 0.55, 0.48, and 0.43 mm, respectively. Their frame rates ( $\sim 200$  Hz) are about twice higher than those of the focused mode and STA. When the frame rate is further increased by 2 folds ( $\sim 400$  Hz), the FWHMs of ME32-StA, CPW32, and CS32-StA are 0.56, 0.55, and 0.43 mm, respectively. As can be observed in the FWHM results, CS-StA keeps the FWHM of STA at different depths. Even if the frame rate is increased to  $\sim 400$  Hz, the FWHM of CS32-StA is still small. The performance of CPW64 is close to that of CS64-StA; however, CPW32 has a larger FWHM than CS32-StA. For the ME-StA method, the FWHM of wire target B is relatively large in the deep regions.

For the hyperechoic target, the CNRs of the focused mode and STA are 2.99 and  $-4.85$  dB, respectively. When the frame rate is increased by twice, the CNRs of ME63-StA, CPW64, and CS64-StA are 0.22, 3.27, and 3.59 dB, respectively. The CNRs of ME32-StA, CPW32, and CS32-StA (with a frame rate of  $\sim 400$  Hz) are  $-1.50$ , 3.48, and 2.84 dB, respectively. According to the CNR results of the hyperechoic region,

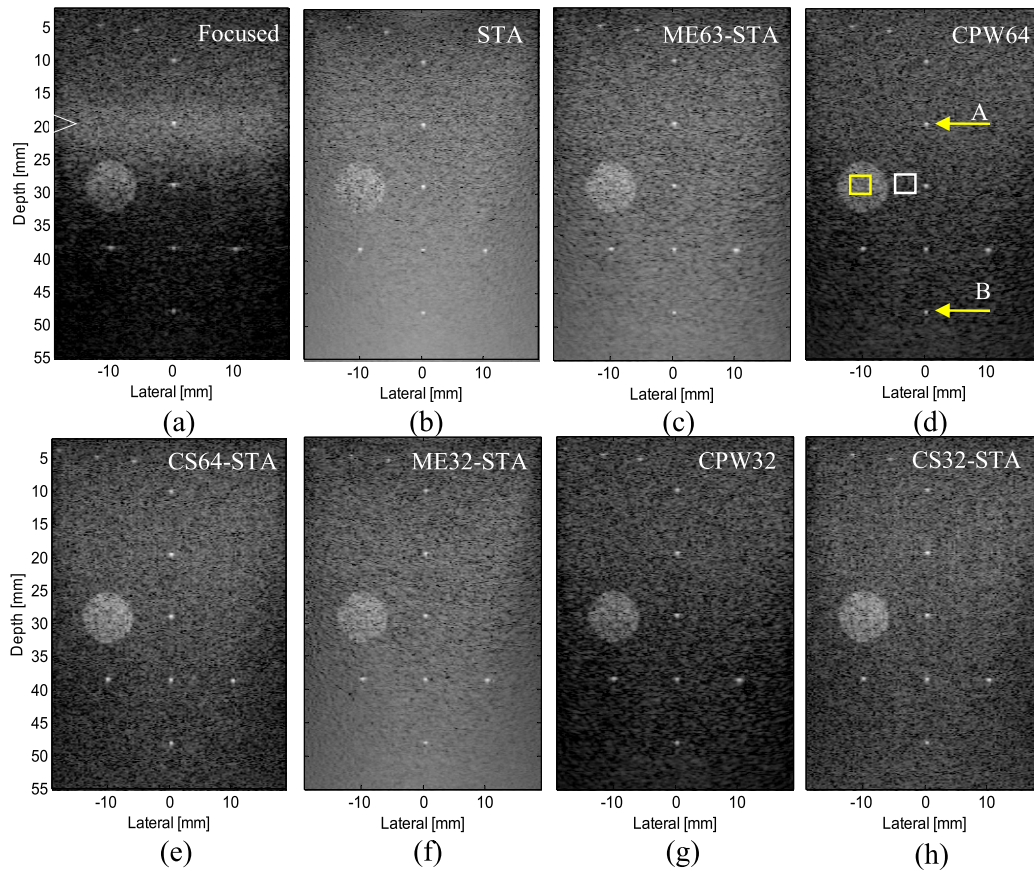


**Fig. 8.** B-mode images of different methods for the wire region of the phantom with a 50 dB dynamic range. The white arrow in (a) indicates the focal depth for the focused method. The yellow arrows in (d) indicate the wire used to calculate the full width at half-maximum. The yellow and white rectangular boxes in (d) indicate the hyperechoic region and its corresponding background region used to calculate the contrast-to-noise ratio.

**TABLE I**

THE FULL WIDTH AT HALF-MAXIMUM (FWHM [mm]) AND CONTRAST-TO-NOISE RATIO (CNR [dB]) FOR DIFFERENT METHODS

Method	Voltage [V]	Frame rate [Hz]	FWHM [mm]		CNR [dB]		
			Wire A	Wire B	Hyperechoic region	Cyst A	Cyst B
Focused	12	~100	0.44	0.58	2.99	11.95	-6.53
STA	50	~100	0.44	0.43	-4.85	-9.14	-11.69
ME63-STA	50	~200	0.45	0.55	0.22	0.33	-16.38
CPW64	12	~200	0.46	0.48	3.27	9.54	-11.53
CS64-STA	12	~200	0.44	0.43	3.59	6.11	-3.16
ME32-STA	50	~400	0.46	0.56	-1.50	0.14	-16.61
CPW32	12	~400	0.50	0.55	3.48	9.97	-7.48
CS32-STA	12	~400	0.43	0.43	2.84	3.43	-10.82

ME-STA, CPW, and CS-STA are all capable of improving the CNR and frame rate at the same time, and the improvement of ME-STA is the lowest. CS-STA performs better than CPW when the frame rate is about 200 Hz, but worse than CPW when the frame rate is about 400 Hz.

For cyst A, the focused mode and STA produce the highest (11.95 dB) and lowest CNR (−9.14 dB), respectively. When

the frame rate is increased by twice, CPW64 obtains a higher CNR (9.54 dB) than ME63-STA (0.33 dB) and CS64-STA (6.11 dB). All of them can improve the CNR of STA but their CNRs are lower than that of the focused mode (11.95 dB). When the frame rate is increased by four times, the CNRs of ME32-STA, CPW32, and CS32-STA are 0.14, 9.97, and 3.43 dB, respectively. These results have the same trend as



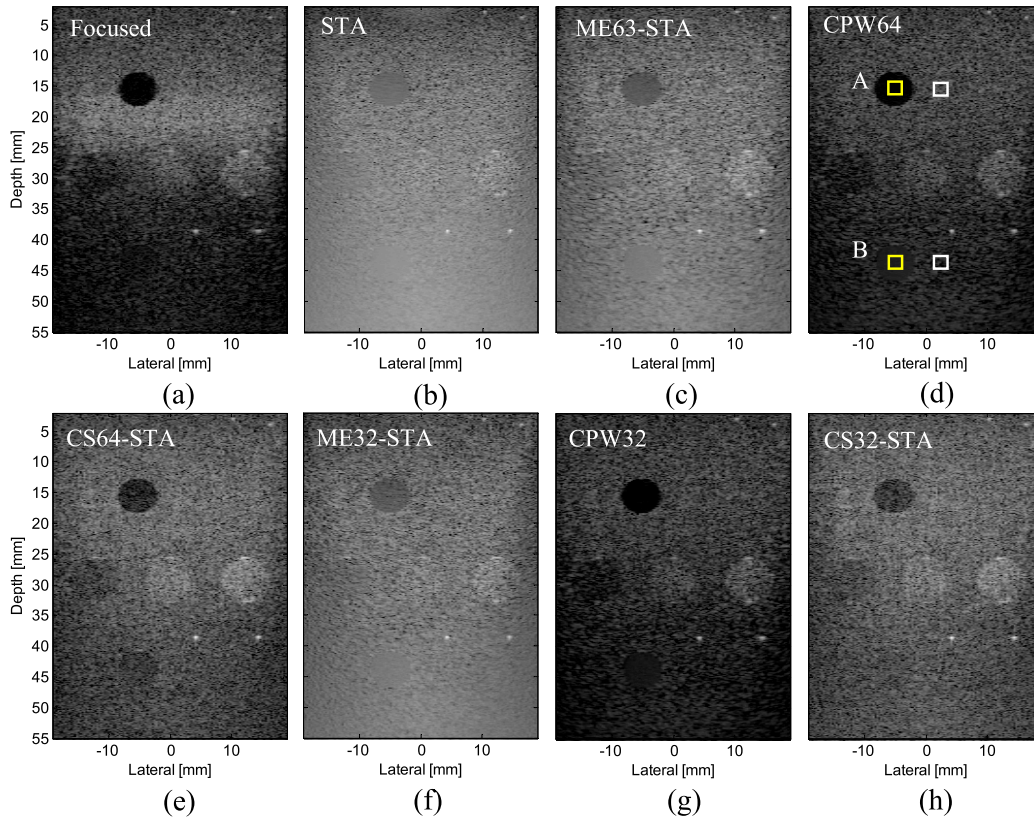


Fig. 9. B-mode images of different methods for the cyst region of the phantom with a 50 dB dynamic range. The white arrow in (a) indicates the focal depth for the focused method. The yellow and white rectangular boxes in (d) indicate the cyst regions and their corresponding background regions used to calculate the contrast-to-noise ratio.

ME63-STA, CPW64, and CS64-STA. From the CNR results of the cyst at the shallow depth (cyst A), it can be seen that ME-STA, CPW, and CS-STA are all capable of improving the CNR and frame rate at the same time. CPW has the best improvement, followed by CS-STA and ME-STA.

For cyst B, the CNRs of the focused mode and STA are  $-6.53$  and  $-11.69$  dB, respectively. When the frame rate is increased by twice, CS64-STA ( $-3.16$  dB) has better CNR performance than ME63-STA ( $-16.38$  dB) and CPW64 ( $-11.53$  dB). When the frame rate is further increased by twice, the CNRs of ME32-STA, CPW32, and CS32-STA are  $-16.61$ ,  $-7.48$ , and  $-10.82$  dB, respectively. As can be seen from the CNR results of the cyst at the deep depth (cyst B), the CNR of the focused mode is not as high as it behaves for cyst A. The CNRs of ME-STA are worse than that of STA, while the CNRs of CS-STA and CPW are better than that of STA. CS-STA performs better than CPW when the frame rate is about 200 Hz, but worse than CPW when the frame rate is about 400 Hz.

#### V. In Vivo EXPERIMENTS

In the phantom experiments, CS-STA achieves good spatial resolution (small FWHM) and contrast resolution (large CNR). However, *in vivo* conditions are much more complicated. For example, tissues may have inhomogeneous acoustic properties such as attenuation and speed of sound. In addition, the relationship between STA and PW is derived from the assumption

of a linear ultrasound system, which does not always hold in real situations.

Despite these potential issues, preliminary *in vivo* experiments on the biceps brachii muscle and thyroid of a healthy human subject were performed with the same Verasonics V1 system and 128-element linear-array transducer. Similar to the phantom experiments, CS-STA was compared with the focused mode, STA, ME-STA, and CPW in the *in vivo* experiments. The focus of the focused mode was at the depth of 16 mm, and other parameters were the same as those in the phantom experiments. In order to ensure similar imaging views, the subject was asked to keep still during the whole acquisition procedure.

The B-mode images of the biceps brachii muscle and thyroid are shown in Figs. 10 and 11, respectively. Compared with the phantom results, the *in vivo* CS-STA images are darker, especially for the thyroid. In spite of this, the results demonstrate that CS-STA is also feasible for the *in vivo* environment. As shown in Fig. 10, the muscle fibers (marked as yellow arrows) in the CS-STA images are as clear as those in the STA image, which verifies again that CS-STA has the capability of keeping the resolution of STA. As the muscle fiber is near the focal region of the focused mode, it is also clearly displayed in the focused image. In contrast, the fibers in the ME-STA and CPW methods do not appear as distinct as those in the focused mode, STA, and CS-STA. In Fig. 11, the STA and ME-STA images are a little blurred, and these blurs barely appear in the focused, CPW, and CS-STA images.

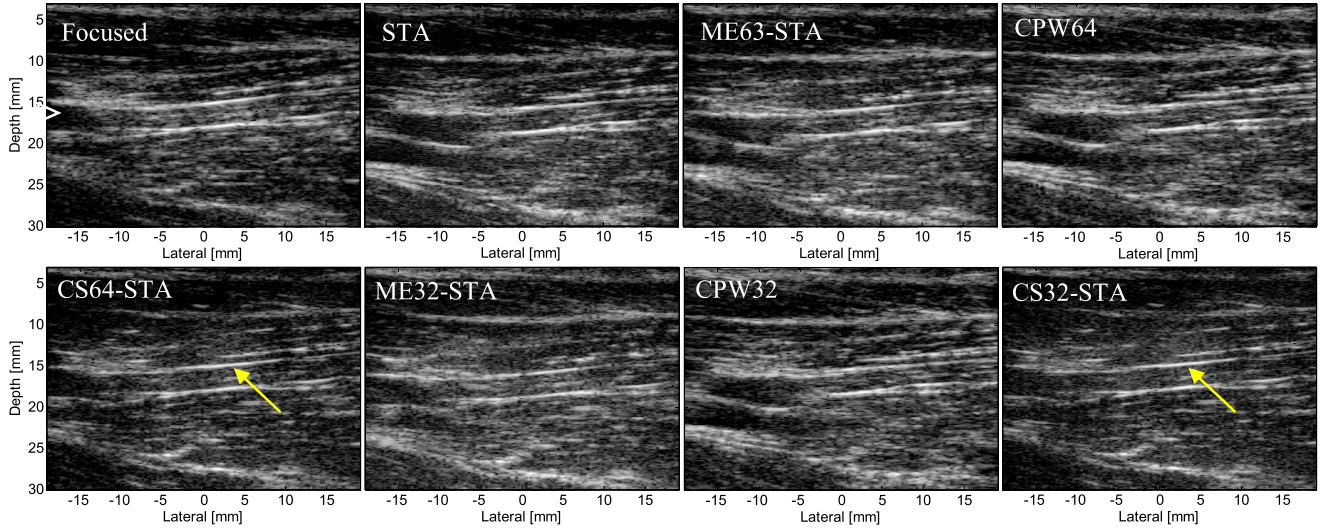


**Fig. 10.** B-mode images of different methods for the biceps brachii muscle of the human subject with a 50 dB dynamic range. The white arrow in (a) indicates the focal depth for the focused method. The yellow arrows indicate the muscle fibers.

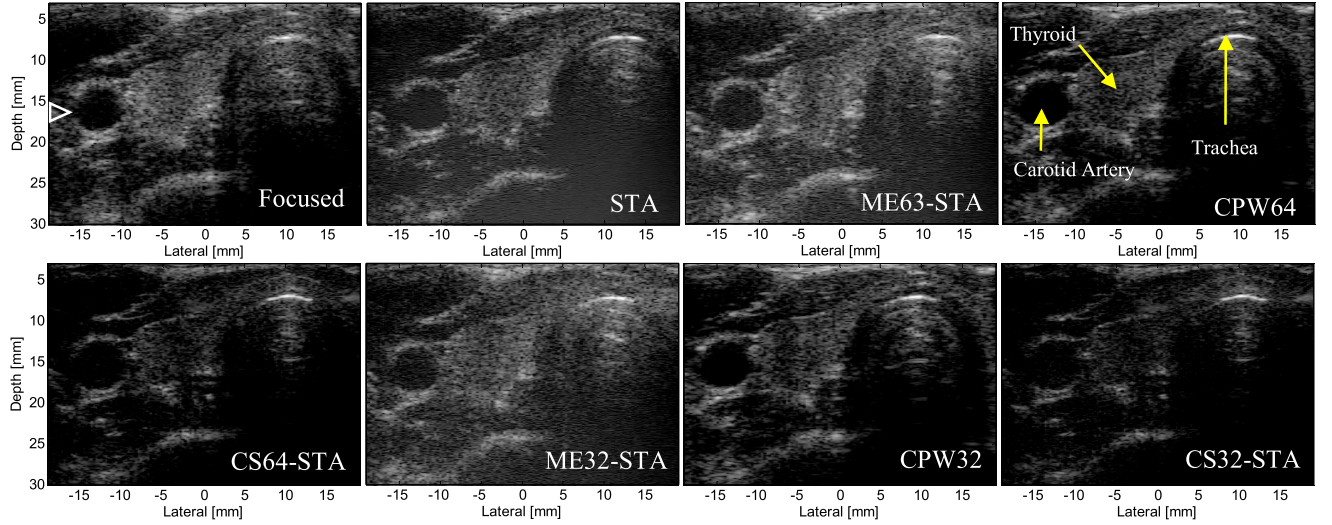


**Fig. 11.** B-mode images of different methods for the thyroid of human subject with a 50 dB dynamic range. The white arrow in (a) indicates the focal depth for the focused method. The yellow arrows indicate the carotid artery and thyroid.

The carotid artery walls and boundaries of the thyroid are clearer in the CS-STA image than in the focused and CPW images. However, the carotid artery lumen in CS32-STA is not as dark as that in the CPW images, in accordance with the CNR results of the cyst region in the phantom experiments. The small difference between the imaging views for different modes in Figs. 10 and 11 are due to inevitable movements and respiration of the subject, because it took more than 10 seconds to transfer the data to the host computer after each imaging mode had been finished.

## VI. DISCUSSIONS

### A. Explanations for the Results

As Table I shows, compared with the focused, ME-STA, and CPW methods, STA achieve the best FWHM performance. CS-STA keeps this advantage with fewer firings. This is

because STA is capable of achieving the full dynamic focusing in both transmission and reception [27] and CS-STA recovers the full STA channel dataset and forms the STA image. Even though STA achieves the best FWHM, it shows low CNR because of the low energy produced by only one element in each STA firing. CS-STA is expected to achieve higher CNR than STA, since all the elements are active and higher energy is transmitted. As confirmed in Table I, both CS64-STA and CS32-STA achieve higher CNR than STA for the hyperechoic region, cyst A, and cyst B. The results demonstrate that CS-STA is capable of keeping the small FWHM of STA and improving its CNR with a higher frame rate. CS-STA is also competitive when compared with the focused, ME-STA, and CPW methods.

The focused method performs well near the focal depth (wire A and cyst A). The FWHMs of wire A for the focused and CS-STA methods are similar and the CNR of cyst A for



the focused method is much higher than that for CS-STA. However, the quality is degraded in the unfocused area (wire B, hyperechoic region, and cyst B). As shown in Table I, the FWHM of wire B for the focused method is larger than that for the CS-STA method. The CNRs of the hyperechoic region and cyst B for CS64-STA is higher than that for the focused mode.

By activating more elements each time, ME-STA can improve the CNR of STA. However, this improvement is not as significant as CS-STA and is at the cost of a larger FWHM.

As shown in Table I, both FWHM and CNR of ME-STA are worse than those of CS-STA. It should be noted that, not as expected, the CNR of cyst B in the ME-STA method is smaller than that in the STA method. This may be because the energy produced by 4 elements is not strong enough to reach the deep region with the consideration of disperse energy of diverging wave in the space.

The comparison between CPW and CS-STA is interesting because both methods transmit plane waves. The difference is that CPW transmits plane waves with different steered angles while CS-STA transmits plane waves with random apodizations. The FWHMs of CPW and CS-STA are similar except for CPW32. The FWHMs of CPW32 are about 0.07 (wire A) or 0.12 mm (wire B) larger than those of CS32-STA. For the relatively deep regions (the hyperechoic region and cyst B), the CNR of CS-STA is higher than that of CPW when the number of firing is 64 and worse when the number of firings is 32. However, CPW performs better in the shallow regions (cyst A) with both 32 and 64 firings. The worse CNR performance of CPW64 at the deep depths is probably because a large steering angle ( $\pm 10^\circ$ ) is used and the energy is not well concentrated at the deep depths. Moreover, this part of energy lowers the energy of the final image because of the average operation during the beamforming step. The CNR can be improved by choosing a smaller steering angle ( $\pm 5^\circ$ ) as CPW32 implements. However, the smaller steering angle also increases the FWHM, which can be seen from Table I. The better performance of CPW than CS-STA in the shallow depths can be explained by the effective energy. With the same (maximum) voltage of 12 V, the mean voltage applied for all the elements in CS-STA and CPW is 6 V and 12 V, respectively, since a continuous uniform random apodization with a mean value of 0.5 is applied in CS-STA. When the energy of steered plane waves is concentrated in the shallow regions, the effective energy of CPW is higher than that of CS-STA. When the applied voltage to CPW is 6 V, the CNR of CPW64 for cyst A is 4.75 dB (not shown), which is lower than that of CS64-STA (6.11 dB) with the same mean effective voltage.

As described in Section V, the CS-STA images in the *in vivo* experiments are darker than those in the phantom experiments, especially for the thyroid results. This may be the consequence of a large region of hypoechoic tissues. As shown in the focused and CPW images in Fig. 11, except the hyperechoic tissue of thyroid, most regions of this view are occupied by hypoechoic tissues, such as the lumen of carotid artery and the trachea. Since uniform random apodization is applied, the echoes of randomly apodized PW scattered by the tissues in

this region may be lower than those by the muscle and the CIRS phantom. With these backscattered echoes with low amplitudes, the recovered signals are therefore lower and a relatively darker image is produced.

### B. Reconstruction Time

The computational time for the CS recovery is proportional to the imaging depth, the sampling frequency and the number of receive elements, because the CS recovery is repeated for all the receive elements and sample indexes. When using the SPGL1 solver, it takes about 0.4 seconds to recover the original signal from the measurement signal in Matlab 2013a (The MathWorks, Inc., Natick, MA, USA) on a PC workstation (Intel® Xeon® E5-2687w Processor @3.1 GHz, 32 GB RAM). Therefore, it takes about 30 hours to recover the full STA dataset from CS-STA with a depth of 55 mm, sampling frequency of 30 MHz and 128 receive elements. Because of this time-consuming reconstruction process, it is more suitable to state that CS-STA is capable of achieving higher data acquisition rate instead of frame rate. However, this limitation may be partially solved by using more efficient CS reconstruction algorithms and/or parallel computation as the reconstruction procedure for each receive element and sample is independent. The CS reconstruction algorithm influences the computational time as well. For example, our initial test shows that the orthogonal matching pursuit (OMP) algorithm [39] can significantly accelerate the reconstruction (by about 30 folds) but with lower image quality (not shown). In our latest experiments, the reconstruction process was programmed in parallel in Matlab language on Dell XPS 8500 (Intel(R) Core(TM) i7-3770 CPU @ 3.40 GHz, 8 GB RAM). The modified code ran on 4 cores in parallel and the reconstruction time was reduced from 30 hours to about 6.2 hours. The computational time can be reduced further by using graphics processing unit (GPU). We believe that the reconstruction time will not be an obstacle with the development of algorithm optimization and computers.

### C. Reconstruction Quality

The reconstruction quality is related to the sparse basis  $\Psi$ , the incoherence of  $\Psi$ , the measurement matrix  $\Phi$ , the optimization algorithm, and the tolerated error  $\varepsilon$ . According to the CS theory, when the original signal is represented more sparsely, it can be recovered from fewer samples (or firings in this paper), and the recovery is more precise with the same number of samples (or firings). As a result, the choice of the sparse basis  $\Psi$  is crucial to the reconstruction quality of CS-STA. In this work, we analyzed the sparsity of the slow time signal  $\mathbf{x}$  of the STA data in the *sym8* wavelet [36], Fourier, and wave atoms [40] domains. The sorted normalized sparse representation of  $\mathbf{x}$  for the simulated point-target and cyst phantoms and the biceps brachii muscle and thyroid in these three sparse bases are presented in Fig. 12. Both signals from the simulated and *in vivo* objects show their sparsity and they can be represented more sparsely in the *sym8* wavelet domain than in the other two bases. That is why the *sym8* wavelet was



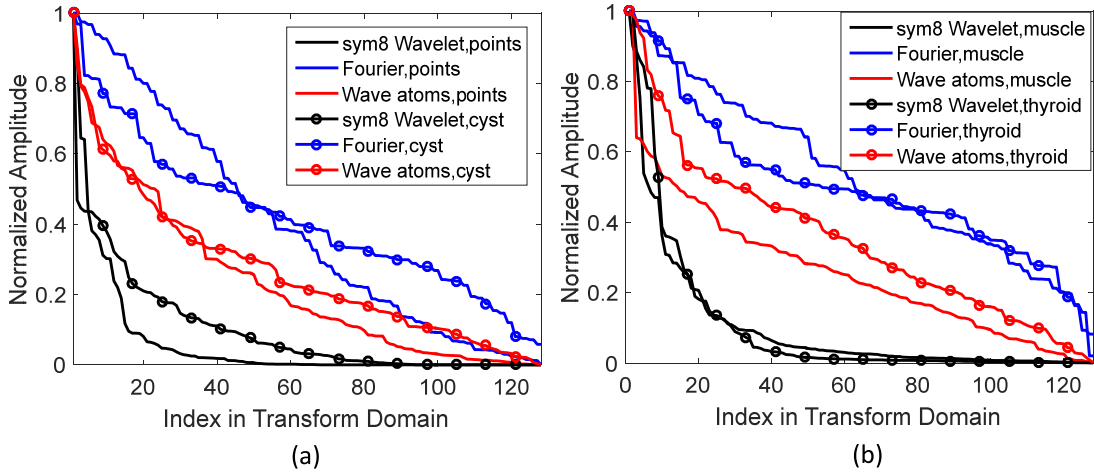


Fig. 12. (a) and (b) are the sorted normalized sparse representations of the slow time signal of STA for the simulated and *in vivo* objects in different sparse bases, respectively. The black, blue, and red lines denote the sparse representations in the *sym8* wavelet, Fourier, and wave atoms domains, respectively.

chosen as the sparse basis in this study. Recently, the over-complete dictionary has been used in the CS application in ultrasound imaging [14]. Because of its optimization process, it allows a much sparser representation. The over-complete dictionary may also be suitable for CS-STA, which needs to be studied further.

In this work, the measurement matrix  $\Phi$  obeys a continuous uniform distribution with amplitudes being randomly distributed in the interval of  $[0, 1]$ . This choice is appropriate for the transmission of an ultrasound transducer array. Another typical random matrix in CS applications in ultrasound imaging can also be a candidate for the transmit apodization of CS-STA. The columns of this matrix have an entry one at a random position and zero elsewhere [21]. With this implementation, only one element is active in each firing, which may reduce the ultrasound energy. To increase the energy, we can activate several elements at random positions for each firing, i.e., the columns of this matrix have several entries one at random positions and zero elsewhere. We did not adopt this method in this work for two reasons. Firstly, the number of active elements should be studied first to comprise the coherence and energy, which increases the complexity of this study. Secondly, the transducer array is not used sufficiently if only part of elements is active. Similar to this matrix, the zero entries can be placed by  $-1$ , which will produce higher energy and utilize the transducer array more sufficiently. However, this kind of transmit apodization cannot be easily implemented in the Verasonics V1 system. As a result, continuous uniform random distribution is used in this work, and the coherence between such a distribution and the *sym8* wavelet sparse basis is about 2.46, close to the coherence 2.2 between the noiselets and Daubechies D4 wavelet [2]. It proves that the continuous uniform random distribution is incoherent with the *sym8* wavelet, which guarantees the successful reconstruction of CS-STA.

In this work, we obtain the sparse representation of the slow time signal of the STA data by solving the convex optimization problem. As Eq. (13) shows, the objective is

minimizing the  $l_1$  norm of  $\mathbf{v}$ . Originally, according to the definition of sparsity, the objective should be minimizing the  $l_0$  pseudo-norm of  $\mathbf{v}$ . However, this process is NP hard. This problem can be solved using  $l_p$  ( $0 < p \leq 1$ ) minimization since the coefficients of sparse representation belong to the  $l_p$  ( $0 < p \leq 1$ ) ball [1]. At the present stage, the  $l_1$  norm instead of  $l_p$  ( $0 < p < 1$ ) pseudo-norm is used considering the convergence time in this work. However, a fast  $l_p$  ( $0 < p < 1$ ) minimization algorithm called iteratively reweighted least-squares with prior information [41] has been adopted in ultrasound signal recovery by choosing the  $p$  value carefully [42]. Considering the well-known knowledge that the  $l_p$  ( $0 < p < 1$ ) minimization is capable of reconstructing the signal with fewer samples than the  $l_1$  minimization [1], the  $l_p$  ( $0 < p < 1$ ) minimization may be an alternative in our further work. Recently,  $l_p$  ( $1 \leq p \leq 2$ ) norm has been employed in the deconvolution of ultrasound imaging since generalized Gaussian distribution is well adapted to the statistics of tissue reflectivities [25]. However,  $l_p$  ( $1 < p \leq 2$ ) norm may not be suitable for CS-STA, which produces a traditional structural B-mode image instead of the statistical information. When solving Eq. (13), the constraint condition is controlled by the tolerated error  $\varepsilon$ .  $\varepsilon = 1 \times 10^{-3}$  in this work. This is an empirical choice compromising the reconstruction quality and reconstruction time. As presented in Section II. B, to process the signals with different amplitudes,  $\mathbf{y}$  is normalized to its  $l_1$  norm before being input to the solver so that the tolerated error is fixed. This procedure is proved to be capable of maintaining the amplitudes of different signals, as Fig. 5 presents. To achieve the same objective, we could also set the tolerated error as a fixed percentage of the  $l_1$  or  $l_2$  norm of  $\mathbf{y}$ . These two approaches share similar normalization idea (normalizing the signal  $\mathbf{y}$  or tolerated error  $\varepsilon$  by the norm of  $\mathbf{y}$ ), and their performance difference will be studied further.

At last, there is a trade-off between the reconstruction quality and the number of firings in CS-STA. This can be seen from the results of CS64-STA and CS32-STA. Nevertheless, implemented with the same number of firings or frame rate,

CS-STA exhibits its higher or comparable image quality to other methods. Furthermore, the reconstruction algorithm has an influence on the reconstruction quality and will be studied in the future. Moreover, in this paper, the recovered STA channel dataset is beamformed with the conventional DAS method. Adaptive beamforming methods (such as minimum variance beamforming) introduce data-dependent coefficients during the summation stage and can improve the performance of beamforming [43]. It should be noted that CS-STA is applied in the stage of channel data recovery while adaptive beamforming is applied in the stage of beamforming. They may be combined together to further increase the image quality, which is our ongoing work. Adaptive beamforming can be adopted in PW imaging to improve its image quality as well. Whether it can obtain better or comparable results compared with CS-STA is an open question and will be investigated in the future.

#### D. Comparison With Other CS Methods

As introduced in Section I, there are two other main methods to improve the frame rate using the CS technology. The first one is to randomly sample the imaging lines of the focused mode, as proposed by Quinsac *et al* [13]; and the second one is to solve the ultrasonic inverse scattering problem, as proposed by Schiffner *et al* [15]. Here, we provide a brief comparison between CS-STA and these two methods in terms of the CS implementation and their performance.

In CS-STA, the linear measurement relationship is derived from the channel data of plane wave and STA firings, and then the measurement matrix  $\Phi$  consists of the transmit apodization of each PW firing. By using double precision float data type (8 bytes) and 128-element array, the memory consumptions of  $\Phi$  for CS64-STA and CS32-STA are therefore 64 KB and 32 KB, respectively. In Quinsac's method, the measurement matrix  $\Phi$  consists of 0 and 1. For an ultrasound image consisting of 128 imaging lines, if 64 imaging lines are sampled randomly, the number of rows and columns of  $\Phi$  will be 64 and 128, which have the same size as CS64-STA. For each row of  $\Phi$ , only one entry is occupied with 1 and others are 0. As a result, the memory consumption of  $\Phi$  for Quinsac's method is 0.5 KB (1/128 of CS64-STA). In Schiffner's method, when the lattice size  $N$  is about 240,000 ( $N_x \approx 400$ ,  $N_z \approx 600$ ), the number of frequency components is about 1,000, and the number of elements is about 128, the memory consumption of  $\Phi$  is about 458 GB [15]. Recently, Schiffner *et al* analyzed the potential of fast multipole method (FMM) in reducing the size of  $\Phi$ . The results show that by choosing appropriate parameters, FMM is capable of reducing the memory consumption from 460 GB to 1.13 GB [44]. From the above descriptions, it can be seen that the measurement matrix  $\Phi$  of CS-STA and Quinsac's method is much smaller in size and they are easier to implement. Although CS-STA occupies relatively low memory space in terms of the measurement matrix, it should be kept in mind that CS-STA needs a much larger numbers of CS reconstructions when compared with the other two methods. If the complexity of each CS reconstruction is comparable for

these three methods, CS-STA will consume much more time.

The performance concerns the frame rate and image quality. As introduced in Section I, the backscattered echoes can be acquired with a single plane wave firing. With these backscattered echoes, the ultrasound image can be reconstructed based on the linear measurement relationship established by Schiffner *et al*. As a result, Schiffner's method is capable of achieving ultrafast ultrasound imaging [15]. Compared with Schiffner's method, the improvements of the frame rate in CS-STA and Quinsac's method are limited because more firings are needed. Experimentally, we could not compare the image quality of these three methods with our imaging parameters at the present stage because of the large memory consumption of  $\Phi$  and undetermined parameter control (e.g., the number of frequency components for a given probe, the lattice size for a given imaging depth and number of subsets in FMM) in Schiffner's method. Nevertheless, a qualitative comparison can be conducted based on the thyroid image of CS64-STA in Fig. 11 and the reported thyroid results [13], [26]. It can be seen that all of them have shown their potential in maintaining the tissue structure and necessary diagnostic information but on different degrees. In Quinsac's method [13], we can observe that the information of unsampled image lines is not maintained as well as that of fully sampled imaging lines and therefore degrades the image quality. If neglecting the difference of the probes and acquisition systems, we can find that the thyroid boundaries of CS-STA appear to be clearer than those of Schiffner's method [26]. However, a more comprehensive comparison with the same probe and acquisition system should be performed.

## VII. CONCLUSION

This paper introduces a new compressed sensing sampling strategy based on the linear measurement relationship between the channel data of plane wave and synthetic transmit aperture firings. Compressed sensing based synthetic transmit aperture is thus proposed to reduce the number of firings and increase the frame rate of ultrasound imaging. Simulations, phantom experiments and preliminary *in vivo* experiments are performed to validate the feasibility and advantages of the proposed method. The results demonstrate that CS-STA is capable of increasing the frame rate while keeping the high resolution of STA and improving its contrast.

## REFERENCES

- [1] D. L. Donoho, "Compressed sensing," *IEEE Trans. Inf. Theory*, vol. 52, no. 4, pp. 1289–1306, Apr. 2006.
- [2] E. J. Candès and M. B. Wakin, "An introduction to compressive sampling," *IEEE Signal Process. Mag.*, vol. 25, no. 2, pp. 21–30, Mar. 2008.
- [3] M. Lustig, D. Donoho, and J. M. Pauly, "Sparse MRI: The application of compressed sensing for rapid MR imaging," *Magn. Reson. Med.*, vol. 58, no. 6, pp. 1182–1195, Jun. 2007.
- [4] G.-H. Chen, J. Tang, and S. Leng, "Prior image constrained compressed sensing (PICCS): A method to accurately reconstruct dynamic CT images from highly undersampled projection data sets," *Med. Phys.*, vol. 35, no. 2, pp. 660–663, Feb. 2008.
- [5] Z. Guo, C. Li, L. Song, and L. V. Wang, "Compressed sensing in photoacoustic tomography *in vivo*," *J. Biomed. Opt.*, vol. 15, no. 2, p. 021311, Mar. 2010.

- [6] M. Cikes, L. Tong, G. R. Sutherland, and J. D'hooge, "Ultrafast cardiac ultrasound imaging: Technical principles, applications, and clinical benefits," *JACC Cardiovascular Imag.*, vol. 7, no. 8, pp. 812–823, Aug. 2014.
- [7] J. Luo and E. E. Konofagou, "High-frame rate, full-view myocardial elastography with automated contour tracking in murine left ventricles *in vivo*," *IEEE Trans. Ultrason., Ferroelect., Freq. Control*, vol. 55, no. 1, pp. 240–248, Jan. 2008.
- [8] J. Udesen, F. Gran, K. L. Hansen, J. A. Jensen, C. Thomsen, and M. B. Nielsen, "High frame-rate blood vector velocity imaging using plane waves: Simulations and preliminary experiments," *IEEE Trans. Ultrason., Ferroelect., Freq. Control*, vol. 55, no. 8, pp. 1729–1743, Aug. 2008.
- [9] G. R. Lockwood, J. R. Talman, and S. S. Brunke, "Real-time 3-D ultrasound imaging using sparse synthetic aperture beamforming," *IEEE Trans. Ultrason., Ferroelect., Freq. Control*, vol. 45, no. 4, pp. 980–988, Jul. 1998.
- [10] L. Tong, H. Gao, and J. D'hooge, "Multi-transmit beam forming for fast cardiac imaging—A simulation study," *IEEE Trans. Ultrason., Ferroelect., Freq. Control*, vol. 60, no. 8, pp. 1719–1731, Aug. 2013.
- [11] G. Montaldo, M. Tanter, J. Bercoff, N. Benech, and M. Fink, "Coherent plane-wave compounding for very high frame rate ultrasonography and transient elastography," *IEEE Trans. Ultrason., Ferroelect., Freq. Control*, vol. 56, no. 3, pp. 489–506, Mar. 2009.
- [12] M. Karaman, P.-C. Li, and M. O'Donnell, "Synthetic aperture imaging for small scale systems," *IEEE Trans. Ultrason., Ferroelect., Freq. Control*, vol. 42, no. 3, pp. 429–442, May 1995.
- [13] C. Quinsac, A. Basarab, and D. Kouamé, "Frequency domain compressive sampling for ultrasound imaging," *Adv. Acoust. Vibrat.*, vol. 2012, Apr. 2012, Art. no. 231317.
- [14] O. Lortintu, H. Liebgott, M. Alessandrini, O. Bernard, and D. Friboulet, "Compressed sensing reconstruction of 3D ultrasound data using dictionary learning and line-wise subsampling," *IEEE Trans. Med. Imag.*, vol. 34, no. 12, pp. 2467–2477, Dec. 2015.
- [15] M. F. Schiffner and G. Schmitz, "Fast pulse-echo ultrasound imaging employing compressive sensing," in *Proc. IEEE Ultrason. Symp. (IUS)*, Oct. 2011, pp. 688–691.
- [16] Q. Zhang, B. Li, and M. Shen, "A measurement-domain adaptive beamforming approach for ultrasound instrument based on distributed compressed sensing: Initial development," *Ultrasonics*, vol. 53, no. 1, pp. 255–264, Jan. 2013.
- [17] G. David, J.-I. Robert, B. Zhang, and A. F. Laine, "Time domain compressive beam forming of ultrasound signals," *J. Acoust. Soc. Amer.*, vol. 137, no. 5, pp. 2773–2784, May 2015.
- [18] C. Wang *et al.*, "An easily-achieved time-domain beamformer for ultrafast ultrasound imaging based on compressive sensing," in *Proc. 37th Annu. Int. Conf. IEEE Eng. Med. Biol. Soc. (EMBC)*, Aug. 2015, pp. 7490–7493.
- [19] R. Tur, Y. C. Eldar, and Z. Friedman, "Innovation rate sampling of pulse streams with application to ultrasound imaging," *IEEE Trans. Signal Process.*, vol. 59, no. 4, pp. 1827–1842, Apr. 2011.
- [20] N. Wagner, Y. C. Eldar, and Z. Friedman, "Compressed beamforming in ultrasound imaging," *IEEE Trans. Signal Process.*, vol. 60, no. 9, pp. 4643–4657, Sep. 2012.
- [21] H. Liebgott, R. Prost, and D. Friboulet, "Pre-beamformed RF signal reconstruction in medical ultrasound using compressive sensing," *Ultrasonics*, vol. 53, no. 2, pp. 525–533, Feb. 2013.
- [22] J. Richey, D. Friboulet, A. Bernard, O. Bernard, and H. Liebgott, "Blood velocity estimation using compressive sensing," *IEEE Trans. Med. Imag.*, vol. 32, no. 11, pp. 1979–1988, Nov. 2013.
- [23] R. van Sloun, A. Pandharipande, M. Misch, and L. Demi, "Compressed sensing for ultrasound computed tomography," *IEEE Trans. Biomed. Eng.*, vol. 62, no. 6, pp. 1660–1664, Jun. 2015.
- [24] C.-H. Chiu and M.-L. Li, "Compressive-sensing like grating-lobe suppressed image reconstruction for photoacoustic linear array imaging," in *Proc. IEEE Int. Ultrason. Symp. (IUS)*, Sep. 2014, pp. 1277–1279.
- [25] Z. Chen, A. Basarab, and D. Kouamé, "Compressive deconvolution in medical ultrasound imaging," *IEEE Trans. Med. Imag.*, vol. 35, no. 3, pp. 728–737, Mar. 2016.
- [26] M. F. Schiffner and G. Schmitz, "Compensating the combined effects of absorption and dispersion in plane wave pulse-echo ultrasound imaging using sparse recovery," in *Proc. IEEE Int. Ultrason. Symp. (IUS)*, Jul. 2013, pp. 573–576.
- [27] J. A. Jensen, S. I. Nikolov, K. L. Gammelmark, and M. H. Pedersen, "Synthetic aperture ultrasound imaging," *Ultrasonics*, vol. 44, pp. e5–e15, Dec. 2006.
- [28] J. Liu, Q. He, and J. Luo, "Compressed sensing for high frame rate, high resolution and high contrast ultrasound imaging," in *Proc. 37th Annu. Int. Conf. IEEE Eng. Med. Biol. Soc. (EMBC)*, Aug. 2015, pp. 1552–1555.
- [29] O. Couture, M. Fink, and M. Tanter, "Ultrasound contrast plane wave imaging," *IEEE Trans. Ultrason., Ferroelect., Freq. Control*, vol. 59, no. 12, pp. 2676–2683, Dec. 2012.
- [30] J. A. Jensen and N. B. Svendsen, "Calculation of pressure fields from arbitrarily shaped, apodized, and excited ultrasound transducers," *IEEE Trans. Ultrason., Ferroelect., Freq. Control*, vol. 39, no. 2, pp. 262–267, Mar. 1992.
- [31] J. A. Jensen, "A model for the propagation and scattering of ultrasound in tissue," *J. Acoust. Soc. Amer.*, vol. 89, no. 1, pp. 182–190, Jan. 1991.
- [32] E. J. Candès, J. Romberg, and T. Tao, "Robust uncertainty principles: Exact signal reconstruction from highly incomplete frequency information," *IEEE Trans. Inf. Theory*, vol. 52, no. 2, pp. 489–509, Feb. 2006.
- [33] E. van den Berg and M. P. Friedlander, (2007). *SPGL1: A Solver for Large-Scale Sparse Reconstruction*. [Online]. Available: <https://www.math.ucdavis.edu/~mpf/spgl1/index.html>
- [34] E. van den Berg and M. P. Friedlander, "Probing the Pareto frontier for basis pursuit solutions," *SIAM J. Sci. Comput.*, vol. 31, no. 2, pp. 890–912, Feb. 2008.
- [35] E. van den Berg and M. P. Friedlander, "Sparse optimization with least-squares constraints," *SIAM J. Optim.*, vol. 21, no. 4, pp. 1201–1229, Apr. 2011.
- [36] I. Daubechies, *Ten Lectures on Wavelets*, vol. 61. Philadelphia, PA, USA: SIAM, 1992.
- [37] J. A. Jensen, "Field: A program for simulating ultrasound systems," in *Proc. 10th Nordic-Baltic Conf. Biomed. Imag.*, 1996, pp. 351–353.
- [38] I. Trots, A. Nowicki, M. Lewandowski, and Y. Tasinkevych, "Multi-element synthetic transmit aperture in medical ultrasound imaging," *Arch. Acoust.*, vol. 35, no. 4, pp. 687–699, 2010.
- [39] Y. C. Pati, R. Rezaifar, and P. S. Krishnaprasad, "Orthogonal matching pursuit: Recursive function approximation with applications to wavelet decomposition," in *Proc. Conf. Rec. 27th Asilomar Conf. Signals, Syst. Comput.*, Nov. 1993, pp. 40–44.
- [40] L. Demanet and L. Ying, "Wave atoms and sparsity of oscillatory patterns," *Appl. Comput. Harmon. Anal.*, vol. 23, no. 3, pp. 368–387, Nov. 2007.
- [41] C. J. Miosso, R. V. Borries, M. Argàez, L. Velazquez, C. Quintero, and C. M. Potes, "Compressive sensing reconstruction with prior information by iteratively reweighted least-squares," *IEEE Trans. Signal Process.*, vol. 57, no. 6, pp. 2424–2431, Jun. 2009.
- [42] A. Achim, A. Basarab, G. Tzagkarakis, P. Tsakalides, and D. Kouamé, "Reconstruction of ultrasound RF echoes modeled as stable random variables," *IEEE Trans. Comput. Imag.*, vol. 1, no. 2, pp. 86–95, Jun. 2015.
- [43] J. F. Synnevag, A. Austeng, and S. Holm, "Adaptive beamforming applied to medical ultrasound imaging," *IEEE Trans. Ultrason., Ferroelect., Freq. Control*, vol. 54, no. 8, pp. 1606–1613, Aug. 2007.
- [44] M. F. Schiffner and G. Schmitz, "Pulse-echo ultrasound imaging combining compressed sensing and the fast multipole method," in *Proc. IEEE Ultrason. Symp. (IUS)*, Sep. 2014, pp. 2205–2208.